Spin Currents in Ferromagnetic Insulators

We proposed that the spin current can transmit in ferromagnetic insulators by means of a propagating spin wave [1]. By attaching Pt probes on the ferromagnetic insulators Y₂Fe₅O₁₂(YIG), we observed that the electric signal can transmit through the insulators. The Pt probes are used for converting the electric signal to the magnetic signals by using the spin Hall effect.

Manipulating of the spin degrees of freedom is the key issue of the spintronics field. So far, the spin of the conduction electrons in a metallic sample is the carrier of the spin current. However, it is well known that the coherent length of the spin of the conduction electrons is too short to use in electric devices. In this work, we propose the new carrier of the spin current which is realized even in the ferromagnetic insulators (FI). We consider the magnetic excitation, called as a magnon, in the non-equilibrium situation. The coherent length of the magnon is order of several millimeters that is enough long to use in devices. We show that the magnon can carry the angular momentum through sample and can be detected by using the normal metal (NM) probes. By using this spin current, we show that two electrically separated NM probes can communicate each other.

In order to investigate the spin current in ferromagnetic sample theoretically, we focus on the dynamics of the magnetizations. The magnetization dynamics obeys the Landau-Lifshitzs-Gilbert (LLG) equation,

$$\frac{d\mathbf{M}}{dt} = -\gamma\left(\mathbf{M} \times \mathbf{H}\right) + \alpha\mathbf{M} \times \frac{d\mathbf{M}}{dt},$$

where $\mathbf{M}$ is the magnetization of the sample, $\mathbf{H}$ is the effective magnetic field acting on the magnetization, γ is gyromagnetic ratio, α is the Gilbert damping coefficient. $\mathbf{H}$ includes the applied magnetic field, the shaped anisotropic field that comes from the dipole-dipole interaction between unit cells, and the random magnetic field due to the finite temperatures. We consider the thin film sample. Two normal metal (NM) probes are attached to the FI for injecting and detecting the spin current (Fig. 1). The NM probe converts the spin current to the charge current due to the spin-orbit interactions. To formulate the spin injection from NM to FI, we consider the exchange coupling at the interface between NM and FI. After the straightforward calculations, we found

Fig. 2 Transverse components of the magnetization obtained by the numerical simulation. The spin current transmits in the x direction.

that the spin torque term $\tau=\mathbf{M}\times\nabla\mathbf{M}$ acts on the interface of FI. The magnitude of the spin torque is proportional to the applied voltage. By including the spin torque term, we calculate the dynamics of the magnetization. Figure 2 shows the time average of the transverse components of the magnetization. Although the spin torque acts on only the interface of FI and NM, the transverse components appears in whole sample. We found that this component is the evidence of the spin current which is excited by the spin injection of NM. This new concept of the spin current can open a possibility of the new spintronics devices.

References
[1] T. Kajiwara et al, Nature **464**, 262 (2010).

Key Words
Spintronics, Spin Current, Spin Wave

Contact to
Sadamichi Maekawa* (Theory of Solid State Physics Division)
 *Present Address: Advanced Science Research Center, Japan Atomic Energy Agency
   E-mail: maekawa.sadamichi@jaea.go.jp
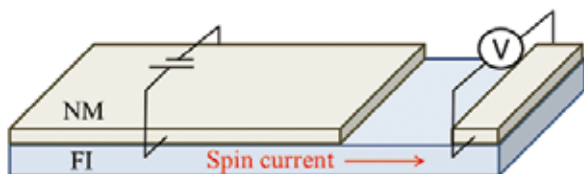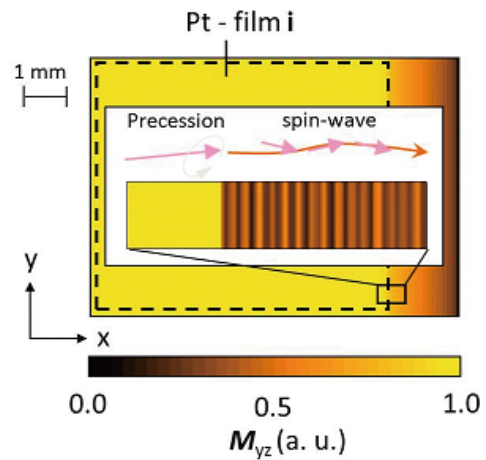   URL: http://asrc.jaea.go.jp/

Fig. 1 Schematic view of the sample configuration. Two normal metal (NM) probes are attached to the Ferromagnetic Insulator (FI). The spin current mediated by the magnon transmits through the FI.

Intrinsic Magneto-Resistance of Metallic Carbon Nanotube

The intrinsic magneto-resistance of the single-walled carbon nanotube (SWNT) is obtained by using a noncontact method. The origin of the magneto-resistance is identified to be the Aharonov-Bohm effect of metallic nanotubes. It is the first clear observation of pure magneto-transport behavior in metallic SWNT.

A single-walled carbon nanotube (SWNT) is a unique conductor with nanoscale diameter. The electronic property of SWNT is governed by the periodic boundary conditions of the wave functions along the tube. Depending on the diameter or helical arrangement, metallic or semiconducting behaviors are expected. Another fascinating feature of the SWNT is the magnetic field effect. When a field is applied parallel to the tube, the quantum states of the electrons are influenced by the so-called Aharonov-Bohm (AB) phase. Namely, the periodic boundary condition depends on the magnetic flux inside the tube and the band gap varies as a function of the magnetic field.

There have been considerable efforts to verify those properties. Indeed, the optical spectroscopy has revealed the splitting of energy gap of semiconducting SWNT caused by the AB effect. In turn, the experimental investigation of AB effect on metallic nanotube is still controversial. It is because the magneto-resistance of SWNT is always contaminated with various extrinsic effects. The crucial difficulty is in the making of good electric contact on a nanotube.

Our concept is to use a contactless method to evaluate the intrinsic magneto-resistance of metallic SWNT. By employing the cavity perturbation technique, high-frequency conductivity of the SWNT can be obtained without making any contact. As is well-known, the cavity resonator has a particular resonant spectrum, which is described by the resonant frequency: f and the quality factor: Q. These two
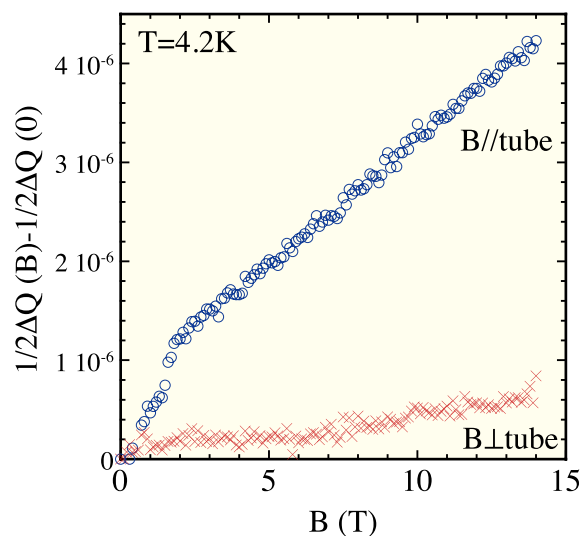

Fig. 2 Magneto-resistance of carbon nanotube for magnetic fields parallel and perpendicular to the tube axis. A large positive magneto-resistance is observed only in the parallel configuration.

factors vary according to the permittivity or conductivity of sample inside the cavity. Thus, high-frequency conductivity of the SWNT can be obtained by comparing f and Q of the cavity with or without the sample.

Figure 2 shows the magneto-resistance evaluated from the field dependence of the inverse Q factor for the highly oriented SWNT thin film at 4.2 K [1]. The tubes are grown by the high-pressure CO conversion method and the average tube diameter is about 0.95 nm. The liner positive magneto-resistance is clearly observed as expected for AB-effect of metallic SWNT. Moreover, the magneto-resistance is completely suppressed in perpendicular condition where magnetic flux does not penetrate inside the tube. The result indicates that he intrinsic magneto-resistance of metallic SWNT is evaluated successfully for the first time. It highlights the powerfulness of microwave technique in investigating nano materials.

References
[1] Y. Oshima *et al*., Phys. Rev. Lett. **104**, 106803 (2010).

Key Words
Carbon Nanotube, Aharonov-Bohm Effect, Magneto-Resistance

Contact to
Hiroyuki Nojiri (Magnetism Division)
E-mail: nojiri@imr.tohoku.ac.jp
URL: http://hfpm.imr.tohoku.ac.jp

Fig. 1 A cylindrical cavity with the resonant frequency around 6.3 GHz used for the cavity perturbation technique to evaluate the intrinsic magneto-resistance of carbon nanotube. The sample is located at the position where the microwave electric field is along the SWNT.

Spin Current and Electrical Signal Transmission in Magnetic Insulator

We present the electric-signal transmission in a magnetic insulator, in which a "spin-wave spin current" is used. An insulator has, in general, a large charge gap, which prevents electron excitation and an electric current. However, in a magnetic insulator, a spin current can flow via spin waves: a spin-wave spin current. Here, we demonstrate that this spin-wave spin current enables an electric-signal transmission even in an insulator, establishing reversible spin transfer processes across a metal/insulator interface.

A flow of spin angular momentum is called a spin current. In a metal the spin current is typically carried by the diffusive motion of conduction electrons (Fig. 1(a)). However, it can also be carried as spin waves—the collective motion of magnetic moments in a material (Fig. 1(b)). Here we call a spin current carried by spin waves a "spin-wave spin current". In a metal, the spin-wave spin current genarally quickly decays—typically within a few microns. In contrast, spin–wave spin currents in magnetic insulators such as $Y_3Fe_5O_{12}$ (YIG) can travel as far as several centimeters.

To make use of the spin-wave spin currents in insulators, it is necessary to find methods of getting a d.c. spin current into and out of the insulators. We used the spin pumping and spin-transfer torque (STT). Spin pumping refers to the transfer of spin angular momentum from magnetization precession motion to conduction-electron spin, a phenomenon which allows generation of a spin current from magnetization motion. STT is, in contrast, the reverse process of this spin pumping, that is, the transfer of angular momentum from conduction-electron spin to magnetization: the magnetization receives torque by absorbing a spin current. These two phenomena enable the mutual conversion of angular momentum between conduction-electron spin and magnetization. However, up to now, experiments on these phenomena have been limited to electric conductors. In the present work, we demonstrate that by using YIG/Pt films, both phenomena occur even at insulator/metal interfaces, and the phenomena allow transmission of a d.c. electric signal through the insulator for a long distance.

First, we established the spin pumping and STT processes at the interface between a magnetic insulator YIG and a paramagnetic metal Pt separately. A microwave was applied to YIG/Pt film in order to inject a spin current into the Pt layer via the spin pumping. The Pt layer is used as a spin-current detector, in which the spin-Hall effect (SHE) converts a spin current into electromotive force. We successfully observed a SHE signal induced by spin pumping from YIG [1]. We then
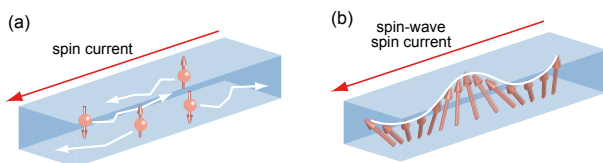

Fig. 1 (a) A schematic illustration of a conduction-electron spin current: spin angular momentum carried by electron diffusion. (b) A schematic illustration of a spin-wave spin current: spin angular momentum carried by collective motion of magnetic moment.
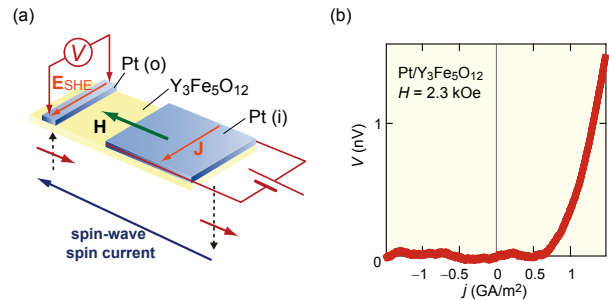

Fig. 2 (a) A schematic illustration of the electric-signal transmission through an insulator. E_{SHE}, **H** and **J** denote electromotive force induced by ISHE, the external in-plane magnetic field and the electric current, respectively. (b) V as a function of the electric-current density in the Pt film. V denotes the voltage difference between the ends of the Pt layer.

applied an electric current to the Pt layer to demonstrate STT across the YIG/Pt interface. In the Pt layer, an electric current induces a spin current via SHE. This spin current exerts STT on the magnetization in YIG, which can be perturbed when magnitude of STT is greater than that of the damping torque. This means that when a sufficient amount of current is applied, the magnetization spontaneously oscillates and emits electromagnetic waves. We attached an antenna on the YIG/Pt film and succeeded in detecting a microwave emission induced by an electric current applied to the Pt film [1].

Finally, we demonstrate the electric-signal transmission in the insulator YIG film by making use of spin transfer across a YIG/Pt interface and spin-wave spin current in YIG [1]. Figure 2(a) shows a schematic illustration of the experimental setup. Two Pt films (**i** and **o**) are sputtered on YIG film and an electric current is applied to the Pt film **i**. The distance between the films **i** and **o** is 1 mm. In this setup, the electric current applied to the Pt film **i** induces magnetization oscillation in the YIG layer due to the STT across the YIG/Pt interface. This magnetization oscillation then propagates in the YIG layer via a spin-wave spin current. When the oscillation reaches the second interface, it generates electric voltage in the Pt film **o** via spin pumping and ISHE. Figure 2(b) shows the voltage difference V between the ends of the Pt film **o** as a function of the electric current density j in the Pt film **i**. When the magnetization of the YIG layer is perpendicular to the electric current, the voltage V signal appears. This hybrid electrical transmission method potentially offers a means of innovative signal delivery in electrical circuits and devices.

Reference
[1] Y. Kajiwara, K. Harii, S. Takahashi, J. Ohe, K. Uchida, M. Mizuguchi, H. Umezawa, H. Kawai, K. Takanashi, S. Maekawa and E. Saitoh, *Nature* (London) **464**, 262 (2010).

Key Words
Spintronics, Spin Current, Spin Transfer

Contact to
Eiji Saitoh (Surface and Interface Research Division)
E-mail: saitoheiji@imr.tohoku.ac.jp

Scanning Tunneling Microscopy/Spectroscopy in Iron-Pnictide Superconductor Ba(Fe$_{0.93}$Co$_{0.07}$)$_2$As$_2$

The recent discovery of high transition temperature (T_c) iron-pnictide superconductor LaFeAsO$_{1-x}$F$_x$ [1] has provided the new route to researches on high-T_c superconductivity. To understand the electronic structure and the mechanism of the superconductivity in high-T_c iron-based pnictide superconductors, scanning tunneling microscopy/spectroscopy (STM/STS) experiments have been performed on Ba(Fe$_{0.93}$Co$_{0.07}$)$_2$As$_2$ single crystals [2].

STM/STS measurements [2] were performed on the cold-cleaved surface of Ba(Fe$_{0.93}$Co$_{0.07}$)$_2$As$_2$ single crystals [3] at 4.9 K in the ultrahigh vacuum (UHV, $P \sim 10^{-10}$ Torr) condition. The STM images indicate two kinds of atomic arrangements: (i) the square lattice structures with the distance of ~ 5.4 Å (i.e., $\sqrt{2} \times \sqrt{2}$ structure) and (ii) the one-dimensional stripe-like structures. Since the former surface does not show the superconducting tunneling spectra, we focus on the superconductivity on the latter surface below.

Figure 1(a) shows a STM topographic image of the one-dimensional stripe-like structures. The stripe-like structures have a periodicity of ~ 7.97 Å which corresponds to twice the As-As (or Ba-Ba) distance (a = 3.96 Å). Figure 1(b) shows the tunneling conductance (dI/dV) spectra measured at different positions along the stripe-like structure. The tunneling spectra exhibit a superconducting energy gap 2Δ, a clear coherence peak, and an asymmetric background at $|V| > \Delta$. The energy gap 2$\Delta \sim$ 15.2 meV is extracted from the distance between the coherence peaks. The single gap structure is consistent with the previous STM/STS results but is different from the multiple gaps ($\Delta \sim$ 7 meV and ~ 4.5 meV) reported by angle resolved photoemission spectroscopy (ARPES).

In this study, the gap ratio is estimated to be 2$\Delta/k_BT_c \sim$ 7.3 in Ba(Fe$_{0.93}$Co$_{0.07}$)$_2$As$_2$. The value is about two times larger than that of the weak coupling s-wave BCS superconductors (2Δ/k_BT_c = 3.53) and is close to that of cuprate superconductors (2$\Delta/k_BT_c \sim$ 6-10). The results indicate that Ba(Fe$_{0.93}$Co$_{0.07}$)$_2$As$_2$ is in a strong coupling regime and the pairing symmetry is unconventional.

Figure 1(c) indicates tunneling spectra measured at the depression region which is characterized by the one dimensional atomic defect with a typical width of 2a-10a. The tunneling spectra show the strong peak structure at ~ 2.5 meV without any features of superconductivity. The peak spectra can be associated with the scattering resonance peak due to the defect structure and/or the characteristic feature of the next atomic layers (i.e., nonsuperconducting Ba layer).

References

[1] Y. Kamihara, T. Watanabe, M. Hirano, and H. Hosono, J. Am. Chem. Soc. **130**, 3296 (2008).
[2] T. Nishizaki, Y. Nakajima, T. Tamegai, and N. Kobayashi, Physica C, to be published (2010).
[3] Y. Nakajima, T, Taen, and T. Tamegai, J. Phys. Soc. Jpn. **78**, 023702 (2009).

Key Words

Scanning Tunneling Microscopy/Spectroscopy, High-T_c Iron-based Pnictide Superconductors, Energy Gap

Contact to

Terukazu Nishizaki (Low Temperature Physics Division)
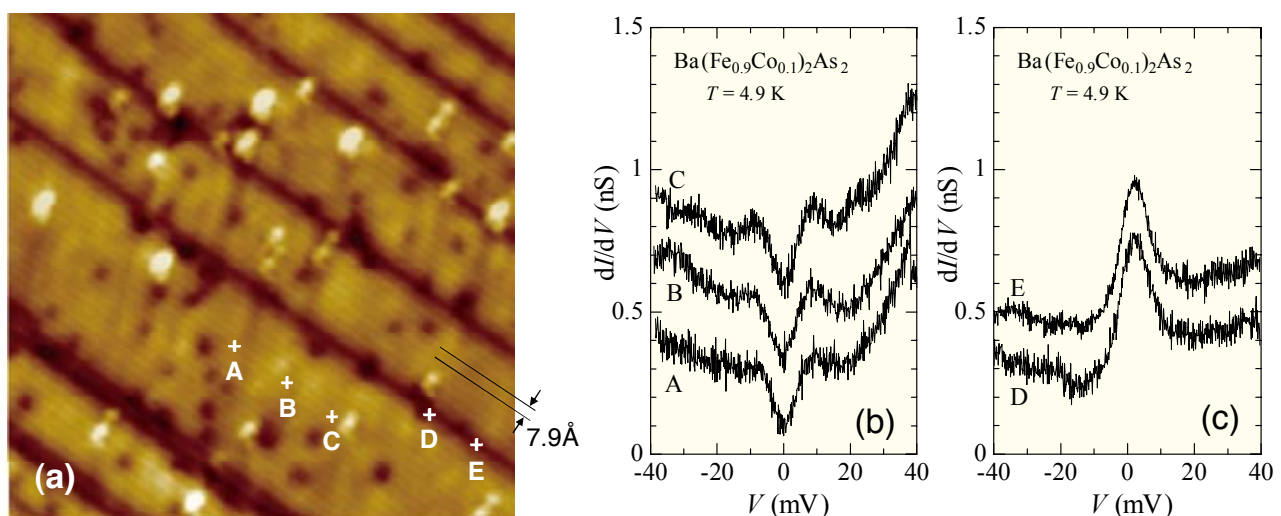 E-mail: terukazu@imr.tohoku.ac.jp
  URL: http://ltp.imr.tohoku.ac.jp/index.htm

Fig. 1 (a) Constant-current STM image of Ba(Fe$_{0.93}$Co$_{0.07}$)$_2$As$_2$ with one dimensional structure. V = 100 mV, I = 20 pA, 390 Å × 390 Å. Tunneling spectra taken at (b) the positions A, B, C and (c) positions D, E marked in (a). Each subsequent spectrum is offset for clarity.

Electric Field Induced Superconductivity at 15 K

The electric double layer capacitor at the interface between an electronic conductor and an ionic conductor has an ability of high density charge accumulation reaching 8×10^{14} cm^{-2}, which is almost two orders of magnitude larger than conventional solid capacitors. By using an electric double layer as a gate dielectric of a transistor, we demonstrated an electric field induced superconductivity occurring at a critical temperature of 15 K, on atomically flat surface of a layered material, ZrNCl. This result indicates an emergence of novel materials science under extremely high electric field.

The electric double layer formed at an electrochemical interface between liquid and solid is recently attracting considerable interest from the view point of charge capacitor applications. However, its ability of high density charge accumulation can be used as a transistor with high capacity and high maximum carrier density. Importantly, the mechanism of the charge accumulation at the electric double layer is electrostatic, providing a novel opportunity to search for new states of matter, which are not accessible by conventional chemistry. We named this transistor, electric double layer transistor (EDLT).

In 2008, we succeeded in demonstrating the first electric field induced superconductivity in an oxide semiconductor, SrTiO$_3$, in a tight in-house collaboration with Prof. Kawasaki's group (WPI), Prof. Nojima's group (IMR), and Prof. Aoki's group (Physics) [1]. Although this work is conceptually important, it is of very limited applicability to materials science as it dealt with the very special case of a material which becomes superconducting at very low carrier densities and for which atomically flat surfaces can be easily fabricated. To generalize this technique to a broader range of materials, we have employed ionic liquid (Fig. 1 right), which was found to exhibit an electrostatic charge accumulation of 8×10^{14} cm^{-2} [2]. This value is eight times larger than the case of a polymer electrolyte used for the demonstration of SrTiO$_3$-EDLT. Another key technique required for EDLTs is the preparation of atomically flat surfaces of solid semiconductors, since it works as a carrier transport channel. For easy preparation of atomically flat surfaces, we chose a layered material, ZrNCl, and introduced a mechanical cleavage method, used in the
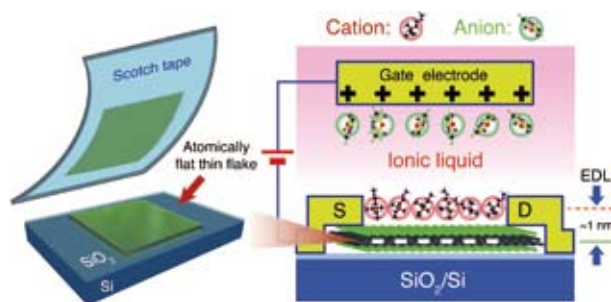

Fig. 1 Left: a micro cleavage technique with Scotch Tape for making atomically flat flakes of single crystals of layered materials. Right: an EDLT device using ionic liquid.
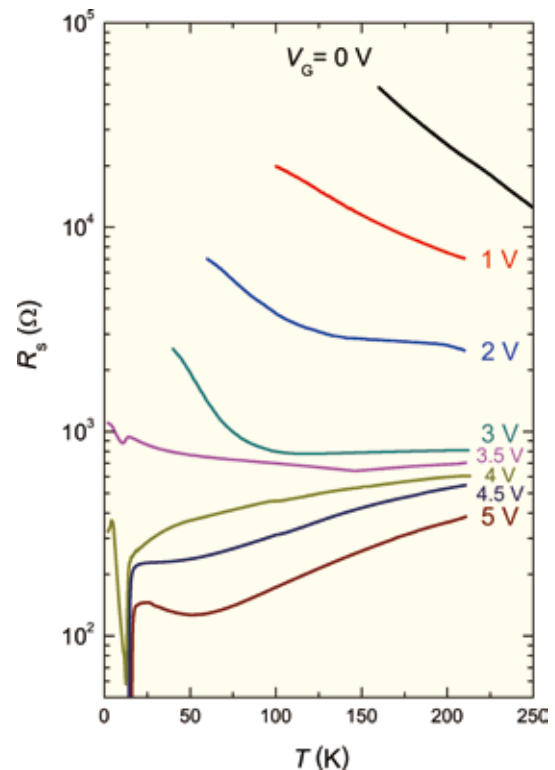

Fig. 2 Temperature dependence of resistivity of a ZrNCl-EDLT for various gate voltages.

fabrication of graphene devices (Fig. 1 left).

Figure 2 displays temperature dependence of resistivity of a ZrNCl single crystal flake of the 12 monolayers in thickness. With increasing gate voltage V_G, the resistivity displays a dramatical reduction. At $V_G = 3.5$ V, we found a resistivity drop, followed by zero resistivity above $V_G = 4$ V, providing convincing evidence for the occurrence of electric field induced superconductivity [3]. T_c is much higher than the case of SrTiO$_3$. The result implied that the EDLT could be a versatile tool applicable to variety of materials and thus could be useful for searching for new superconductors.

Reference
[1] K. Ueno et al., *Nat. Mater.* **7**, 855 (2008).
[2] H. T. Yuan et al., *Adv. Funct. Mater.* **19**, 1046 (2009).
[3] J. T. Ye et al., *Nat. Mater.* **9**, 125 (2010).

Key Words
Electric Double Layer Transistor, Superconductivity, Ionic Liquid

Contact to
Yoshihiro Iwasa* (Low Temperature Condensed State Physics Division)
 * Present Address: Quantum-Phase Electronics Center, University of Tokyo
   E-mail: iwasa@ap.t.u-tokyo.ac.jp

A New CZ Method for Ge Crystals with Extremely Low Dislocation Density

A new CZ method for growing Ge crystals with an extremely low dislocation density was explored. A Ge melt was partially covered with liquid B_2O_3 only in the outer surface region of the melt. GeO_2 particles generating dislocations in the grown crystal were removed by the B_2O_3-covered melt. From a particle-free "melt-window" in the central portion of the melt, Ge single crystals with extremely density were successfully grown.

Recently, there is a renaissance of interest in germanium (Ge) for possible use in the next generation of high-speed ULSI due to its superior carrier mobility in semiconductor industries, as well as low temperature processing [1]. Its application as substrates for GaAs solar cells is also investigated as it enables higher energy-conversion efficiency than Si [1]. For use, Ge is expected free from dislocations to avoid their demerit as severe carrier killers in GaAs epitaxial layers. Since Ge and GaAs well lattice-match (~ 0.12%), dislocation-free Ge crystals are desirable for the substrates with that purpose. Currently, large-sized dislocation-free Ge crystals are grown by the Czochralski (CZ) method in Umicore, world-wide Belgium company. However, it is commercially well recognized that growth of dislocation-free Ge crystal is very difficult. Germanium oxide (GeO_2) particles floating on the Ge melt surface attach to the Ge crystal during growth, resulting in generation of dislocations. The melting point of GeO_2 is 1115˚C, higher than that of Ge (938˚C). They may be formed in the melt originating from the surface oxide layer of charged Ge raw material, air leakage of the chamber or residual moisture in the growth furnace. We explored a new CZ method for growing Ge crystals with an extremely low dislocation density using boron oxide (B_2O_3) with controlling or preventing such particle formation on the melt surface [2].

Figures 1(a)–(c) illustrate the arrangement of Ge, B_2O_3 and the silica crucible in charging, melting and growing stages, respectively. First, B_2O_3 melted at 480˚C, and then Ge melted at 938˚C. Due to fine wetting ability between B_2O_3 and silica glass, the Ge melt and B_2O_3 liquid maintained the arrangement shown in Fig. 1(b). Only the outside region of the Ge melt was partially covered with the liquid B_2O_3. Particles were caught by the liquid B_2O_3 and move outside of the Ge melt surface with the B_2O_3 liquid. Finally, a clean Ge melt surface free from any particles is realized in the central region of the crucible, making it possible to grow from such a
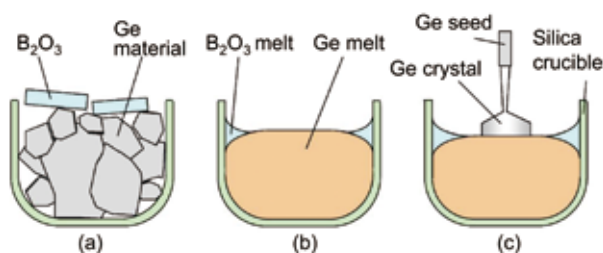

Fig. 2 A photograph of a Ge single crystal grown from B_2O_3-partially-covered Ge melt.

"clean" Ge melt as shown in Fig. 1(c).

Figure 2 shows a photograph of a Ge boule grown from Ge melt partially covered with B_2O_3. The diameter is about 1 inch and the length about 50 mm. Three habit lines were clearly observed. The dislocation density at the top of the crystal shown in Fig. 2 was evaluated by the preferential etching method to be almost zero.

The crystal was n-type and the resistivity, carrier concentration and electron mobility were 18 Ωcm, 6.8×10^{14} cm^{-3} and 3.2×10^3 cm^2/Vs, respectively. B and O concentrations in the grown crystals were lower than the detection limit (2×10^{15} cm^{-3}) in the SIMS analysis, implying that the contamination level of B from B_2O_3 liquid is very low. Any negative influences of B_2O_3 liquid on chemical and electrical properties were not detected.

One of the reasons why B_2O_3 liquid does not dissociate to B and O, and is stable on Ge melt may be that the Gibbs standard free energy of B_2O_3 formation is the lowest among those of isolated B, O atoms and GeO_2 at a temperature close to the melting point of Ge [3]. In the present method, B_2O_3 is being used as a remover of GeO_2 floating on the Ge melt. Its use is very effective for reduction of grown-in dislocation density. This effect can be also originating in wetting ability and low reactivity among Ge melt, silica crucible and B_2O_3 liquid. Realization of complete dislocation-free Ge crystal growth is now in progress.

References

[1] B. Depuydt, A. Theuwis and I. Romandic, Mater. Sci. Semicond. Process. **9**, 437 (2006).
[2] T. Taishi, Y. Ohno and I. Yonenaga, J. Crystal Growth **311**, 4615 (2009).
[3] H. Okamoto, In: T.B. Massalski (Ed.), Binary Alloy Phase Diagrams, 2nd. Vol. 2, 1976 (1990).

Key Words
Germanium, Dislocation-Free, Czochralski Growth

Contact to
Ichiro Yonenaga (Physics of Crystal Defects Division)
  E-mail: yonenaga@imr.tohoku.ac.jp
  URL: http://lab-defects.imr.tohoku.ac.jp/

Fig. 1 Illustrations of arrangement of Ge, B_2O_3 and silica crucible: (a) after charging, (b) after melting and (c) during the growth.

Quantum Transport Properties in Nanoscale Materials by First-Principles Calculations

Transistor density of silicon-based semiconductor chips is approaching the ultimate size limitation. Innovative materials such as organic molecules, single-walled carbon nanotubes, and graphenes have been suggested as substitutions of conventional semiconductors to implement promising electronic devices in nanoscale where quantum mechanics dominates the electron kinetic behavior. The present work showed an interesting behavior of quantum conductance, which is based on nanoscale-structured material. The method used in these papers is based on the nonequilibrium Green's function and the code has been developed originally in our research group. All the numerical calculations have been conducted by using the HITACHI SR11000 supercomputing system at the Center for Computational Materials Science, IMR.

A systematic analysis of electron transport characteristics for 1D heterojunctions with two nitrogen-doped (N-doped) capped carbon nanotubes (CNTs) facing one another at different conformations is presented considering the chirality of CNTs (armchair(5,5) and zigzag(9,0)) and spatial arrangement of N-dopants. Figure 1 shows schematic illustration of the two facing N-doped armchair CNTs in different sites. The remarkable feature emerging from the I-V characteristics of the N-doped CNT junctions is that the tunneling current between two N-doped capped CNTs is dramatically increased by N-doping and negative differential resistance (NDR) behavior is observed as in the Esaki-like diode, that is, tunneling diode. The *ab initio* calculations show that the modification of the molecular orbitals by the N-dopants generates a conducting channel in the designed CNT junctions. The facing conformation and the N-doping site significantly affect electron transport characteristics; when the N-doped CNT junction has the pentagon-facing conformation and a nitrogen atom is substituted at the cap region, especially the b doping site (See Fig.1), it provides strong NDR behavior with large peak-to-valley ratio and V_{peak} values. Furthermore, a clear interpretation is presented for the NDR behavior by a rigid shift model of the HOMO- and LUMO-filtered energy levels in the left and right electrodes under the applied biases. It is concluded that the doped nitrogen atom plays an important role in the electron transport characteristics of the designed CNT junctions by modifying their molecular orbitals so as to have NDR behavior. These results give an insight into the design and implementation of various electronic logic functions based on CNTs for applications in the field of nanoelectronics [1].

Structure modulation of graphene nanoribbons (GNRs) is already possible, by using direct focused electron writing or plasma etching. Defects in GNR structures, such as vacancy or doped atoms, are also reported to modify GNR electronic properties significantly. In the present study, we perform an *ab initio* calculation to investigate transport properties of GNR junctions self-consistently with nonequilibrium Green's function approach combined with density functional theory [2]. Here, we fabricate GNR edge defects by removing three carbon atoms from the edges of zigzag GNR, with the dangling bonds saturated by hydrogen atoms (See Fig. 2). We obtain I-V curves of edge-defect junction in modulation of the intensity of transverse electric field. From the results of transport property of an edge-defect ZGNR junction, It is concluded that the tunable tunneling current can be sensitively controlled by transverse electric fields. In the presence of external fields, the junction almost turns off the conducting
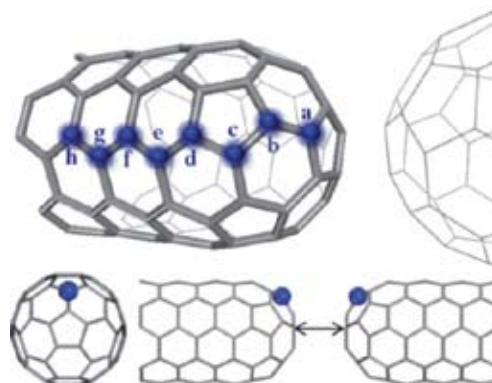

Fig. 1 Schematic of the two facing N-doped capped CNTs in different conformations according to the chirality of the armchair(5,5) CNTs. The NDR behavior significantly depends on the N-doping site and the facing conformations of the N-doped capped CNT junctions.
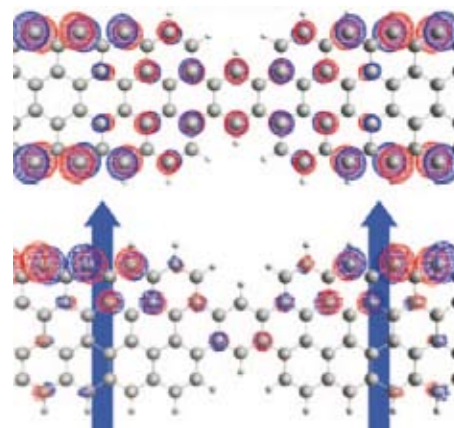

Fig. 2 LUMO of edge-defect graphene nanoribbons junction, with external field indicated by blue arrows.

channel when external field exceeds 1.0 V/Å exhibiting the maximum of the on/off ratio up to 10^4. Consequently, electronic devices based on edge-defect ZGNR junctions have the advantage of easy control through the transverse electrostatic fields. The study of small and narrow GNR devices benefits graphene integrated circuit engineering that might be realized by ultrafine GNR fabrication technologies in the future.

References
[1] S. U. Lee, R. V. Belosludov, H. Mizuseki, and Y. Kawazoe, Small **5**, 1769 (2009).
[2] G. Yin, Y. Y. Liang, F. Jiang, H. Chen, P. Wang, R. Note, H. Mizuseki, and Y. Kawazoe, J. Chem. Phys. **131**, 234706 (2009).

Key Words
Molecular Electronics, Molecular Devices, First Principles Calculations

Contact to
Yoshiyuki Kawazoe (Materials Design by Computer Simulation Division)
    E-mail: kawazoe@imr.edu
    URL: http://www.kawazoe.imr.edu/

3D Analysis of Dopant Distributions in MOSFET Structures by Laser-assisted Atom Probe Tomography

The dopant distributions in metal-oxide- semiconductor field effect transistor (MOSFET) structures (gate, gate oxide, channel, source/drain extension, and halo) were analyzed by laser-assisted atom probe tomography (Laser APT). The segregations of P atoms on the grain boundaries in poly-Si gate and on the interface between gate and gate oxide were observed. B atoms were enriched near the edge of the source/drain extension. These results are very important to understand the origin of variability in MOSFET characteristics.

As the minimum feature size of MOSFET decreases to 65 nm or less, variability in MOSFET characteristics has become a serious problem. The major factor is supposed to be inhomogeneous distribution of discrete dopant in the channel and/or gate region. Therefore, the information on the exact location of each dopant in the channel region is strongly desired. In this work, we report dopant distributions over entire regions of an n-type MOSFET structure with atomic scale resolution using Laser APT (IMAGO: LEAP3000XHR) [1].

The samples were long gate length n-type MOSFETs (line-and-space pattern), consisting of a poly-Si gate, a gate oxide film, and a Si substrate with source/drain extension and halo regions. After B atoms were implanted into the channel region, the gate-oxide film and P-doped poly-Si gate were formed. The sample was then patterned and etched by conventional lithography and dry etching with the gate length of 60 nm. As and B atoms were implanted for a source/drain extension and punch-through-stopper, respectively, followed by spike annealing at 1,050°C to activate the implanted dopants.

A 3D elemental map of the line-and-space pattern sample is shown in Fig. 1(a). A cross-sectional transmission electron microscopy image is also shown in Fig. 1(b). The observed region in Fig. 1(a) corresponds to the region inside the broken line in Fig. 1(b). The MOSFET structure, which consists of a poly-Si gate electrode, gate oxide, Si channel, and source/drain extension, was clearly observed. Elemental maps of P in a 10-nm-thick slice parallel to the X-Z plane are shown in Fig. 1(c). P atoms were not uniformly distributed in the poly-Si gate electrode due to the segregation on grain boundaries in the poly-Si gate, at the interface between the poly-Si gate and the gate oxide [1,2].

In order to clarify the detailed dopant distribution around the source/drain extension, the enlarged view of 3D elemental map, in which the edge of the source/drain extension was nearly in the center of the needle specimen, is shown in Fig. 2. B atoms were enriched near the edge of the source/drain extension because the B atoms were implanted (halo) after extension implantation for the punch-through-stopper. These results are very important to understand the origin of variability in MOSFET characteristics, especially in threshold voltage fluctuation.
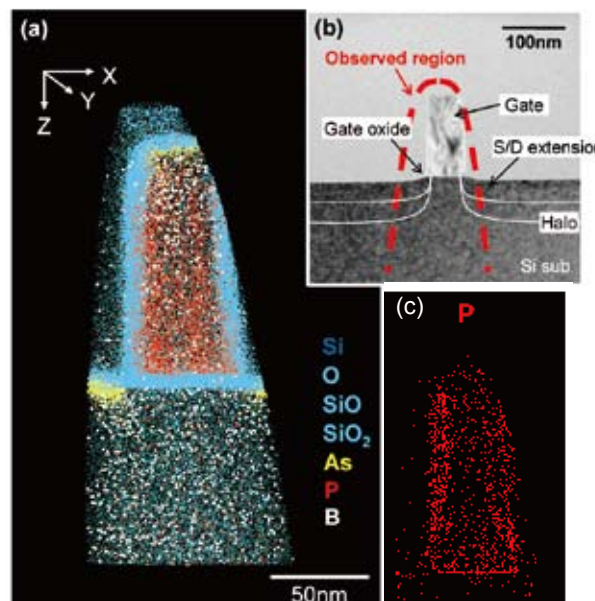

Fig. 1 The 3D elemental map of an n-type MOSFET from a line-and-space pattern sample. (b) Cross-sectional transmission electron microscopic image. (c) Elemental map of P in a slice 10nm thick.
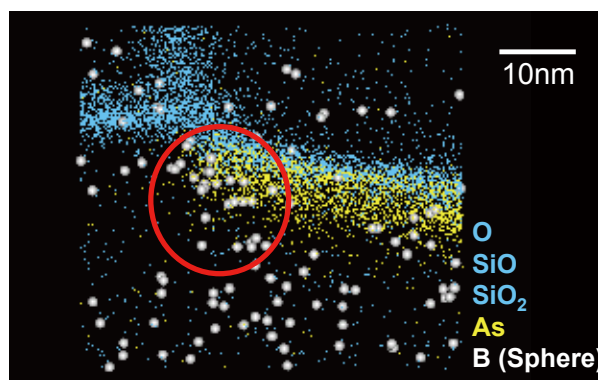

Fig. 2 The enlarged view around the edge of the source/drain extension. Red circle indicates the B enriched region.

References
[1] K. Inoue, F.Yano, A. Nishida, H. Takamizawa, T. Tsunomura, Y. Nagai, M. Hasegawa: Ultramicroscopy 109, 1479 (2009).
[2] K. Inoue, F. Yano, A. Nishida, H. Takamizawa, T. Tsunomura, Y. Nagai, M. Hasegawa, Appl. Phys. Lett. **95,** 043502 (2009).

Key Words
Laser Atom Probe, MOSFET, Dopant Distribution

Contact to
Yasuyoshi Nagai (Irradiation Effects in Nuclear and Their Related Materials Division)
  E-mail: nagai@imr.tohoku.ac.jp
  URL: http://wani.imr.tohoku.ac.jp/

Nitride Semiconductors: Saving Our Planet

Nitride semiconductors such as InN, GaN, AlN and their alloys are very promising for fabricating devices with low energy consumption, high-power, and high-frequency. InGaN-based blue light-emitting-diodes (LEDs) and laser-diodes (LDs) have been already commercially available. The new trends of nitride semiconductors in the region of deep ultraviolet, green, and infrared wavelength, will promote the device applications saving energy and creating new energies. Our researches are related with these new technology trends, challenging the nitride semiconductor-based LDs for the optical fiber communications system, phosphor-free white LEDs, brilliant green LEDs, and high-efficiency solar cells. One of the key tasks for implementing the above devices is to improve the crystalline quality of the InN film, using the pressurized-reactor metalorganic vapor phase epitaxy (PR-MOVPE) technology suitable for mass productions.

The development of sciences and technologies has brought large conveniences to our life, but also problems to our planet, such as the globe warming effect due to the over exhausting of the carbon dioxide. To solve this problem, we have to reduce the energy consumption and create new energies, for example, from solar energy. A strong candidate for these purposes is nitride semiconductor material, which covers the bandgap energy from about 0.63 to 6.03 eV corresponding to the wavelength of 0.21 to 1.97 μm. These series of materials can be used to fabricate new devices which save much more energy, create new energies and are environmental-friendly (free of arsine, phosphorus, selenium, and mercury). For energy saving, we propose solid-state lighting with phosphor-free white LEDs based on nitride semiconductor layers, as shown in Fig.1(a). This structure provides higher emission efficiency than that of the phosphorus type. If all the conventional lighting equipments are substituted by the solid-state-lighting, the reduction of the energy consumption will be about 1/10. On the other hand, for creating new energies, we propose nitride semiconductor-
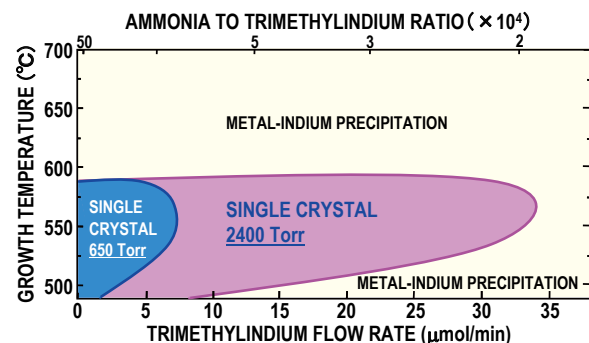
Fig. 2 Phase diagram of InN growth as functions of growth temperature and trimethylindium flow rate at 650 Torr and 2400 Torr.

silicon combined solar-cell structure, that a silicon substrate is sandwiched with high indium composition InGaN and InN layers as shown in Fig.1(b). This cell can cover the whole solar spectrum and lead to a theoretical conversion efficiency of about 36%. In addition, we are exploring the possibility of InN-based laser diodes for optical-fiber communications systems. The temperature stability of InN band-gap is higher than that of InGaAsP, promising for Peltier-free and dense wavelength- division-multiplexing applications.

The above applications require high-quality InN and high indium composition InGaN layers, which are difficult to grow using the conventional low-pressure (LP) and atmospheric-pressure (AP) MOVPE. The barriers lie in the extremely high equilibrium vapor pressure of nitrogen between solid and vapor phases for InN, and the phase separation for InGaN. We have proposed and designed the pressurized-reactor (PR) MOVPE and obtained InN films with extended growth-condition-window as shown in Fig.2 compared with LP and AP-MOVPE [1, 2]. Here, ammonia and trimethylindium (TMIn) as nitrogen and indium sources are used, respectively. PR-MOVPE can be expected to make it possible to further improve the InN and InGaN crystalline quality for device applications.

References

[1] Y. H. Liu, T. Kimura, T. Shimada, M. Hirata, M. Wakaba, M. Nakao, S. Y. Ji, and T. Matsuoka, phys. stat. sol. (c), **6**, S381 (2009).

[2] Y. H. Liu, T. Kimura, Y. T. Zhang, M. Hirata, Masaki Hirata, K. Prasertusk, R. Katayama, and T. Matsuoka, The 37th International Symposium on Compound Semiconductors, FrD1-2 (2010), Takamatsu, Japan, *invited talk*.

Key Words

Nitride Semiconductors, White LEDs, Solar Cells

Contact to

Takashi Matsuoka (Physics of Electronic Materials Division)
   E-mail: matsuoka@imr.tohoku.ac.jp
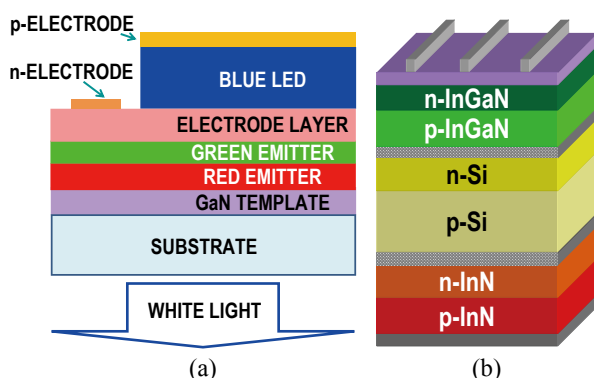   URL: http://www.matsuoka-lab.imr.tohoku.ac.jp/

Fig. 1 A phosphor-free nitride semiconductor-based white LED (a) and a solar cell (b) combined with silicon substrate. For the white LED structure, the current is injected to only blue active layer and its blue light excited green and red active layers.

Observation of Charged Exciton States in ZnO Modulation-doped Quantum Wells

We report on the effect of electrical injection from Ga delta-doped layer of an MgZnO barrier on the magneto-optical properties of a ZnO/MgZnO single quantum well (SQW). Approaching the delta-doped layer to the SQW layer resulted in the photoluminescence (PL) blueshift due to the screening of piezoelectric and macroscopic polarization field by electrons from the MgZnO barriers. Circularly polarized PL was observed in magnetic fields of up to 50 T with a Faraday configuration when the delta-doped layer is located 6 nm away from the SQW layer. The observed Zeeman splitting and the degree of circular polarization in magnetic fields revealed that the PL from the negatively charged excitons (X^-) for the first time in a ZnO system.

Magneto-optical spectroscopy is a spectacular tool in studying the electronic structure in low-dimensional systems [1,2], especially for visualization of the excitation spectrum of Landau quantized states in interface two-dimensional electron states. Recently ZnO has attracted attention in this aspect to look for potential electronic application since the observation of quantum Hall effects. It was also known through spectroscopic research that Coulomb effects between the interface electrons and a hole play an important role. As a prototypical model system where the hole position is well defined, we studied the optical properties of 5-nm-thick modulation-doped ZnO/MgZnO single quantum wells (SQWs) to understand the properties of such an interface (charged) exciton. Circular polarization in PL from the charged exciton was enhanced by a magnetic field up to 50 T with a Faraday configuration at 4.2 K, as shown in Fig. 1(a) and 1(b). The PL peak energies for both polarization components ($\sigma^\pm$) are almost coincident and independent of the magnetic field. Almost zero-splitting of the PL and magnetic-circular dichroism suggest existence of the X^-

states and its importance of Coulomb effects (Fig. 1(c)-(e)). This is a first-time observation of the negatively charged exciton in ZnO-based quantum structures [2]. Based on the detailed analysis, a binding energy of the charge exciton was evaluated to be approximately 5 meV. We also observed magneto-PL from a collective state in a ZnO single heterojunction containing high-mobility electrons. The current postulation has a possibility to be used in a versatile manner to get in-depth insight for the optical properties of other wide-gap oxides [3-5].

References
[1] T. Makino, Y. Segawa, A. Tsukazaki, A. Ohtomo, Appl. Phys. Lett. **93**, 121907 (2008).
[2] T. Makino, Y. Furuta, Y. Segawa, A. Tsukazaki, A. Ohtomo, Y. Hirayama, R. Shen, S. Takeyama, Y. Takagi, M. Kawasaki, Phys. Rev. B **80**, 155333 (2009).
[3] T. Yamasaki, T. Fukumura, Y. Yamada, M. Nakano, K. Ueno, T. Makino, and M. Kawasaki, Appl. Phys. Lett. **94**, 102515 (2009).
[4] H. Hiraga, T. Fukumura, A. Ohtomo, T. Makino, A. Ohkubo, H. Kimura, and M. Kawasaki, Appl. Phys. Lett. **95**, 032109 (2009).
[5] H. Hiraga, T. Makino, T. Fukumura, A. Ohtomo, and M. Kawasaki, Appl. Phys. Lett. **95**, 211908 (2009).

Key Words
Exciton, Modulation-doped Structure, Photoluminescence

Contact to
Takayuki Makino (Superstructured Thin Film Chemistry Division)
E-mail: tmakino@imr.tohoku.ac.jp
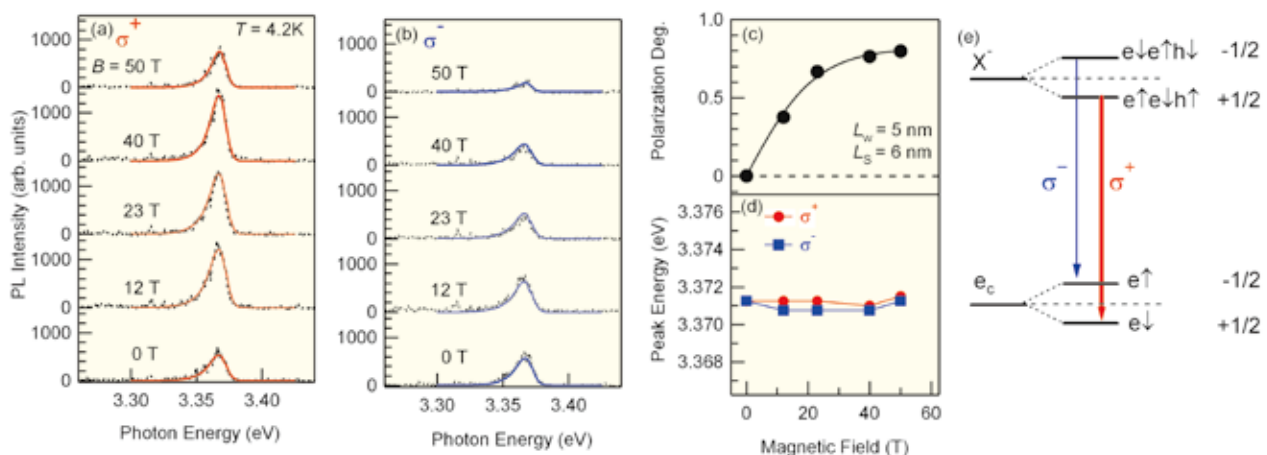URL: http://www.kawasaki.imr.tohoku.ac.jp/English/top.html

Fig. 1 Spectral evolution of PL with the applied magnetic field perpendicular to the QW plane (*B*=0-50 T) in different circular polarizations for modulation-doped ZnO SQW taken at *T*=4.2 K with L_s= 6 nm. (c) Degree of circular polarization (ρ) and (d) the peak energies of the PL spectra in both polarizations. (e) An optical transition model, a charged exciton as an initial state of the emissive transition.

Giant Magnetoresistance and Interface Spin-asymmetry in Co2MnSi/Ag/Co2MnSi Magneto-Resistive Devices

Epitaxial-Co2MnSi/Ag/Co2MnSi current-perpendicular-to-plane magnetoresistive (CPP-GMR) devices were fabricated by UHV magnetron sputtering systems. The maximum MR ratio of about 36% at room temperature was observed, indicating high spin-polarization of Co2MnSi clearly. A quantitative analysis of bulk and interface spin-asymmetry coefficients (β and γ) based on Valet & Fert's model showed a large contribution of spin-asymmetric electron scattering at Co2MnSi/Ag interfaces to the MR effect, which could be originated from good band matching of up-spin electrons between Co2MnSi and Ag (001)-planes.

Half metals, which have perfectly spin-polarized conduction electrons, are very important materials in Spintronics research field, because they are able to enhance various kinds of spin-dependent phenomena such as tunnel and giant magnetoresistance effects, *etc.* CPP-GMR structures, which consist of two ferromagnetic layers separated by a nonmagnetic layer, are promising to observe half-metallicity at room temperature (RT) because electron scattering both in the bulk region and at the interface contributes to the MR effect. In this study, we fabricated the fully epitaxial CPP-GMR devices with a candidate of half-metal Co2MnSi (CMS) and an Ag spacer and investigated the magneto-transport properties systematically.

Figure 1 shows high-resolution TEM images of CMS/Ag/CMS annealed at 350°C. Fully epitaxial growth with very flat and sharp interfaces was clearly confirmed. In CMS/Ag/CMS, it was possible to increase the annealing temperature up to 550°C due to small solubility of Ag with CMS. Finally, we observed maximum MR ratios of 36% and 68% at RT and 100 K, respectively [1], indicating the high spin-polarization of CMS not only at low temperature but also at RT. CMS thickness dependence of resistance change area product (ΔRA) for CMS/Ag/CMS is shown in Fig.2. The contributions from bulk and interface scattering to MR represented by β and γ, respectively, can be quantitatively estimated by the fitting based on Valet-Fert's 2-current model [2]. The fitting result shows γ at the CMS/Ag is very large both at RT and 100K, which contributes dominantly to the large MR ratio. Miura *et al.* [3] calculated a ballistic conductance in a (001)-CMS/Ag/CMS structure and found a large conductance in the majority spin channel in the parallel state. This good band matching can be responsible for the observed large γ and the MR ratio.

Our recent studies on magnetic tunnel junctions based on CMS have also demonstrated the successful tuning of E_F in the half-metallic gap by Al-doping to CMS [4] and the importance of CMS composition to the half-metallicity [5]. Improvement of CMS electrodes will further increase the spin polarization of CMS, and consequently the MR ratio in CPP-GMR at RT.
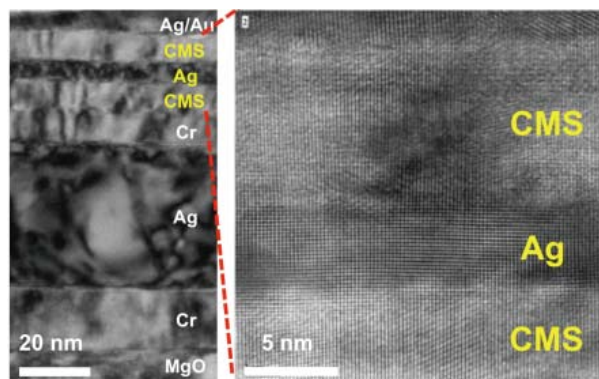

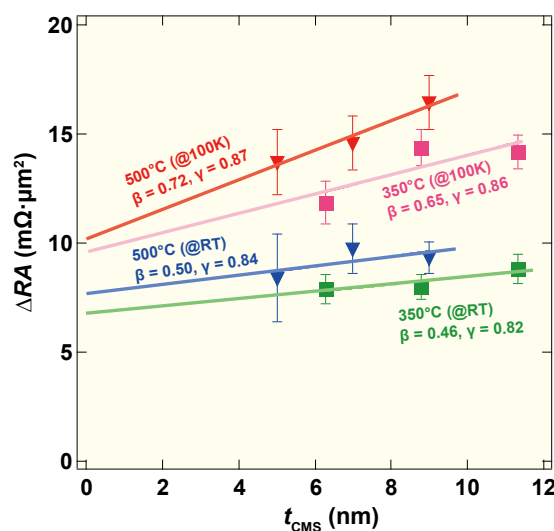Fig. 1 High-resolution TEM image for a CMS/Ag/CMS fully epitaxial film.

Fig. 2 CMS thickness dependence of ΔRA for CMS/Ag/CMS annealed at 350°C (■) and 500°C (▼).

References

[1] T. Iwase, Y. Sakuraba, S. Bosu, K. Saito, S. Mitani, and K. Takanashi. Appl. Phys. Express 2, 063003 (2009).
[2] T. Valet and A. Fert, Phys. Rev. B, **69**, 144413 (2004).
[3] K. Miura *et al*, unpublished.
[4] Y. Sakuraba *et al*., Phys. Rev. B, **81**, 094402 (2010).
[5] Y. Sakuraba *et al*., Appl. Phys. Lett., **96**, 092511 (2010).

Key Words
Spintronics, Half-Metal, CPP-GMR

Contact to
Koki Takanashi (Magnetic Materials Division)
    E-mail: koki@imr.tohoku.ac.jp
    URL: http://www.magmatex.imr.tohoku.ac.jp/~mml/index.html

Remarkable Benefits Obtained When the Congruent Point of a Compound Meets the Stoichiometric Point

We have developed an ideal LiNbO₃ crystal for device applications half a century after the birth of LiNbO₃ in Bell Laboratories. This involved a renovation of Dalton's principles on the stoichiometry of materials, which has been uncritically accepted for two centuries. The simple addition of MgO resulted in the formation of a congruent-melting LiNbO₃ crystal with a stoichiometric structure.

Many oxides, particularly those that have excellent properties for devices, often form solid solutions to some extent and their congruent points differ from their stoichiometric points. $LiNbO_3$ is a typical oxide that has superior optical and piezoelectric properties, but its congruent composition has a Li_2O content of 48.5 mol%, which is slightly lower than that of the stoichiometric composition (50.0 mol%). The congruent composition is ideal for growing crystals because the crystal has the same composition as the source melt. However, because of its nonstoichiometry, congruent $LiNbO_3$ does not have optimal properties for device applications. In contrast, stoichiometric $LiNbO_3$, which is very hard to grow, has an ideal crystal structure in which each element (Li, Nb and O) completely occupies its own site. Consequently, it has excellent physical properties so that it is used in various optoelectronic devices. It has been a long-held dream to make the congruent point of $LiNbO_3$ coincident with its stoichiometric point. However, for over half a century the stoichiometric point of $LiNbO_3$ has been considered to be fixed.

We have discovered a simple solution that involves adding MgO to $LiNbO_3$ powder in the ratio $Li_2O:Nb_2O_5:MgO$ = 45.30:50.00:4.70 [1] and use it as the source melt. Using this method, it is possible to grow an ideal $LiNbO_3$ crystal for device applications, cs-MgO:LN. $LiNbO_3$ has three sites for its three constituent elements (Li, Nb and O). If each site is completely occupied by its element, the crystal will have the stoichiometric structure (s-LN in Fig. 1). This means that each site has an activity of unity in the stoichiometric crystal, and thus the activity of each constituent element will also be unity. The converse is also true, namely if each constituent element has an activity of unity, then the crystal will have the stoichiometric structure. This is a renovation of Dalton's principle of stoichiometry.

We apply this new concept to the development of the ideal $LiNbO_3$ for device applications (i.e., cs-MgO:LN). cs-MgO:LN is located on the isoconcentration line of Nb_2O_5 (Fig. 2) and has unique sites for O and Nb with activities of unity. In contrast, Li, Mg and lattice vacancies occupy the Li site (cs-
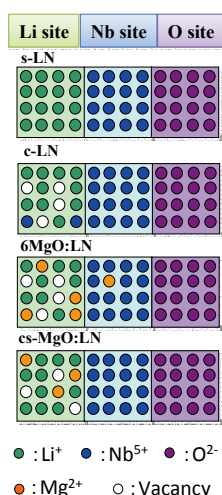

: Li⁺ : Nb⁵⁺ : O²⁻
: Mg²⁺ ○ : Vacancy

Fig. 1 Site occupancies in various lithium niobates including cs-MgO:LN.
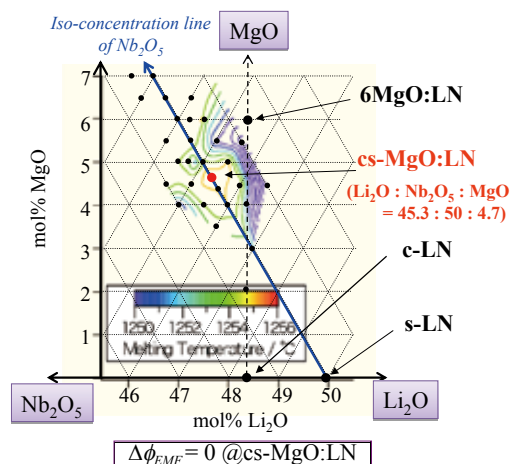

$\Delta\phi_{EMF}= 0$ @cs-MgO:LN

Fig. 2 cs-MgO:LN on the isoconcentration line of Nb_2O_5 has a c-EMF of zero, which demonstrates the realization of both congruency and stoichiometry.
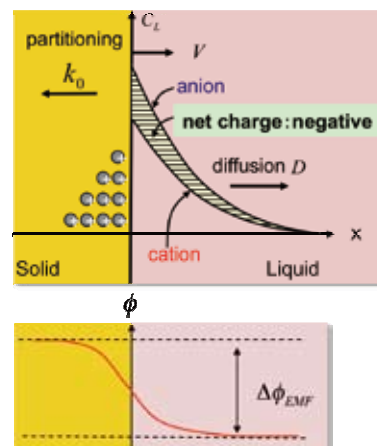

Fig. 3 The occurrence of a crystallization EMF, $\Delta\phi_{EMF}$, due to the segregation of ionic species in the melt near the interface.

MgO:LN in Fig. 1). The question is whether it is possible to make the activities of these elements (including vacancies) unity. The answer is 'yes' by selecting appropriate standard-state chemical potentials for them [2]. This has been demonstrated both analytically and experimentally. We measured the interfacial potential, crystallization electromotive force (c-EMF), caused by segregation of ionic species near the interface (Fig. 3) during crystallization of ionic $LiNbO_3$ melts. cs-MgO:LN has highest melting temperature and a c-EMF of zero, which indicates that there is no segregation at the congruent point. This result demonstrates the simultaneous occurrence of congruency and stoichiometry in cs-MgO:LN.

References
[1] H. Kimura and S. Uda, J. Cryst. Growth, **311**, 4094 (2009).
[2] S. Uda, J. Cryst. Growth, **310**, 3335 (2008).

Key Words
Stoichiometry, Congruent, LiNbO₃

Contact to
Satoshi Uda (Crystal Chemistry Division)
   E-mail: uda@imr.tohoku.ac.jp

3D Imaging of Magnetic Nanoparticles by Electron Tomography

3D shapes and distribution of FePd nanoparticles (NPs) have been studied by single-axis tilt tomography using atomic number (Z) contrast. We demonstrate that weighted back-projection (WBP) yields a better estimation of the particle size in the z-direction than simultaneous iterative reconstruction technique (SIRT) does, most likely because of the presence of a "missing wedge" in the original data set.

Recent developments in ultrahigh density magnetic storage technology rely on novel recording media with a high magnetocrystalline anisotropy energy (MAE), in order to increase storage density and to reduce recording noises. FePd alloy NPs with the L1$_0$-type ordered structure is one of the candidate materials suitable for the ultrahigh density magnetic storage media. Here the atomic ordering is a key issue for improving the hard magnetic properties [1, 2]. Therefore previous studies have focused on the atomic structure inside the NPs. On the other hand, the high-areal density packing of NPs and the control of magnetostatic interaction among the NPs are considered as the next step to realize ultrahigh density magnetic storage media. For this purpose, it is desired to visualize and understand 3D structures of NPs and spatial configuration of neighboring NPs precisely by means of electron tomography.

The FePd alloy NPs studied were formed as epitaxial islands on a NaCl(001) substrate using sequential deposition of Pd and Fe followed by postdeposition annealing. The tilt series of Z-contrast images were obtained using an FEI Titan 80-300 scanning transmission electron microscope (STEM) operating at 300 kV. Alignment of the tilt axis for the obtained data set by an iterative cross-correlation technique and subsequent 3D reconstruction were performed by using the Inspect3D software package. As for the algorithm for 3D reconstruction, we employed WBP, as well as SIRT.

Figure 1 compares reconstructed images processed by WBP (a) and SIRT (b), viewed from an oblique direction [3]. The tilt axis is the x axis, about which the specimen film is sequentially tilted toward the y direction. It is noted that some floating dotlike artifacts, as indicated by the arrows, are seen in the reconstructed image obtained with WBP, while the
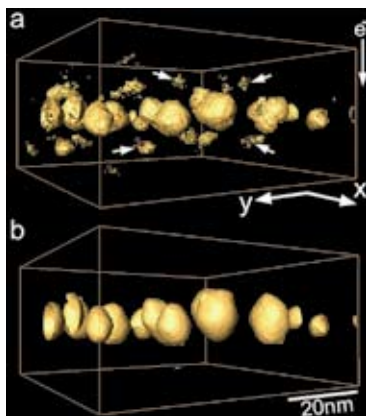

Fig. 1 Oblique-view of the reconstructed volume processed by WBP (a) and SIRT (b). Large discrepancy in particle thickness (height) is apparent between these two images. For 3D reconstruction, 81 images taken at tilt angles between -66° and +64° were employed.
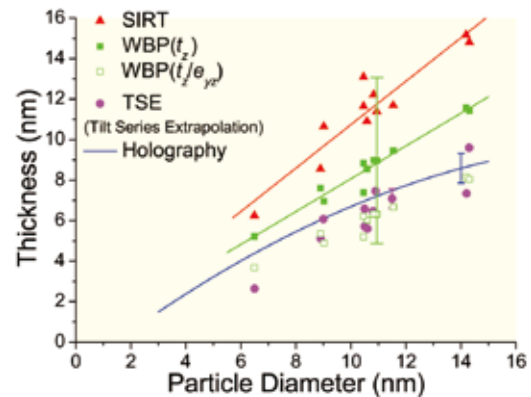

Fig. 2 The relation between particle diameter and thickness (height) for the FePd NPs estimated by using several different techniques. The elongation factor (e_{yz}) is 1.42 for the present experimental conditions.

result by the SIRT shows a smooth surface with little apparent artifacts. Besides the floating artifacts, a significant difference between these two images can be noticed. NPs in the upper image show oblate 3D-shapes, while those in the lower image are prolate.

To examine a possible elongation of a reconstructed particle height in the z direction, we therefore measured projected particle length in the y direction as a function of tilt angle and deduced the true particle height by extrapolating the projected length to the value expected at the tilt angle α = 90°.

Using the aforementioned procedure, here termed "tilt-series extrapolation (TSE) method", we obtained a relation, which summarizes the relation between particle diameter and thickness estimated by using several different techniques (Fig.2). Note that the deduced thicknesses obtained by the TSE agree well with those obtained by WBP (t_z / e_{yz}) as well as those by electron holography. On the other hand, the thicknesses suggested by SIRT are much larger than the values deduced by the TSE method or electron holography. Therefore, within a framework of single-axis tilt geometry, it is demonstrated in a semiquantitative manner that the WBP gives a better result in terms of the accuracy of the particle length in the z direction than that predicted by SIRT [3]. It is demonstrated that TSE method is found to be reliable and useful in order to examine the accuracy and resolution of 3D reconstructed information provided by different algorithms.

References
[1] K. Sato, Nature Mater. **8**, 924 (2009).
[2] A. Kovács, K. Sato et al., Phys. Rev. Lett. **103**, 115703 (2009).
[3] K. Sato, K. Aoyagi, and T. J. Konno, J. Appl. Phys. **107**, 024304 (2010).

Key Words
Electron Tomography, 3D Structure, Nanoparticle

Contact to
Kazuhisa Sato (Advanced Analysis of Materials Division)
  E-mail: ksato@imr.tohoku.ac.jp

Observation of Magnetic Excitation in Quantum Spin System at J-PARC

Entire excitation spectrum of the quantum spin system CuGeO₃ was successfully observed by using the new chopper spectrometer 4SEASONS in J-PARC. This demonstration opens up the possibility of study on complex dynamics in the strongly correlated electron systems, which plays an important role for the emergence of new functions.

In strongly correlated electron systems, new phenomena can appear due to the complex combination among degrees of freedom of electron (charge, spin and orbital). To understand the mechanism, it is important to obtain the information of not only basic structure but also the dynamics in intriguing materials, which is strongly coupled with electrons. For the study of dynamics, neutron-scattering experiments, which can measure the collective behavior of spins or nuclei in a system, provide important information.

However, up to now, because of the insufficient intensity of available neutron beam, the observation of excitation spectrum was limited in a part of energy-momentum space. In order to make a progress in the study of dynamics by the neutron-scattering measurement, we developed a new method, which can efficiently collect the date with several different experimental conditions. We have first attempted the method to the observation of spin excitation spectrum in a quantum spin system CuGeO₃, on the chopper spectrometer 4SEASONS installed in J-PARC [1]. The sample used in the experiment was assembled single crystals with the total weight of ~30 grams. (See Fig.1)

As clearly seen in Fig. 2, in a single measurement, the entire spectrum of two-spinon continuum was detected above the low-lying mode. This observation is consistent with the previously obtained result at the ISIS facility in UK, which used to provide the most intense pulsed neutron beam when the first high-energy neutron-scattering measurement on CuGeO₃ was done [2]. Moreover, the intensity map with the lower incident neutron energy and better experimental
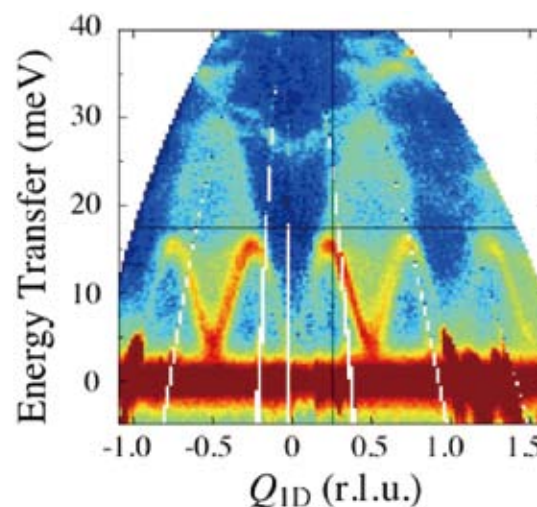

Fig. 2 Spin excitation spectrum in the quantum spin system CuGeO₃. Color indicates the measured neutron intensity. Whole excitation continuum of two-spinon was successfully observed in a wide energy-momentum space.

resolution, which was collected at the same time, indicates an opening of spin gap (E_g~2meV) due to a formation of spin singlet below 14K. (Not shows.)

The simultaneous observation of entire and detailed structure of excitation spectrum is expected to be effective for the exploration of complex dynamics originated from a coupling among plural degrees of freedom of the electron in a condensed matter. With focusing on a study of spin excitations and phonons in high-transition-temperature superconductivity, we are developing the technique of neutron-scattering measurement at J-PARC.

References

[1] M. Nakamura, R. Kajimoto, Y. Inamura, F. Mizuno, M. Fujita, T. Yokoo, and M. Arai, J. Phys. Soc. Jpn. **78**, 093002 (2009).

[2] M. Arai, M. Fujita, M. Motokawa, J. Akimitsu, and S. M. Bennington, Phys. Rev. Lett. **77**, 3649 (1996).

Key Words
Neutron-scattering Measurement, Quantum Spin System, Spin Excitation

Contact to
Masaki Fujita (Materials Processing and Characterization Division)
 E-mail: fujita@imr.tohoku.ac.jp
 URL: http://www.imr.tohoku.ac.jp/jpn/research/bumon/m_proces/06.html

Fig. 1 Assembled single crystals of the spin-Peierls compound CuGeO₃.

AC Impedance Analysis of a Ni-Nb-Zr-H Glassy Alloy with Femtofarad Capacitance Tunnels

A Nyquist diagram of a $(Ni_{0.36}Nb_{0.24}Zr_{0.40})_{90}H_{10}$ glassy alloy shows a semi-true circle, indicating that it is a conducting material with a total capacitance of 17.8 μF. The Bode plots showing the dependencies of its real and imaginary impedances, and phase on frequency suggest a simpler equivalent circuit having a resistor in parallel with a capacitor. Dividing the total capacitance (17.8μF) by the capacitance of a single tunnel (0.9fF), we deduced that this material has a high number of dielectric tunnels, which can be regarded as regular prisms separated from the electric-conducting distorted icosahedral $Zr_5Ni_5Nb_3$ clusters by an average of 0.225 nm [1].

Following the discovery of the Coulomb blockade effect by quantum-dot tunneling at low temperature, a number of studies have reported the achievement of room-temperature oscillation. Recently, Fukuhara *et al*. have observed the electric current-induced voltage oscillation in $((Ni_{0.6}Nb_{0.4})_{0.7}Zr_{0.3})_{1-y}H_y$ glassy alloys (with $0.052 \leq y \leq 0.152$) at temperatures below 240 K [2] and at room temperature [3]. Thus, we regarded it as a DC/AC converting device with a large number of nanometer size capacitors.

To investigate the distribution state of vacancies in eccentric glassy alloys, we determined an AC impedance of a glassy alloy consisting of nanometer-sized clusters [4]. Significantly, no research work has been carried out previously on the AC impedance analysis of Ni-Nb-Zr-H glassy alloys with femtofarad capacitances. Our results indicate that the glassy alloys have potential applications as nonwired, room-temperature quantum devices such as batteries, amplifiers, and memory switches.

To nondestructively analyze electronic contribution of the glassy alloy without grain boundaries, we measured the AC impedance in a simple circuit in which the specimen was integrated at room temperature, as a function of the applied frequency. The Nyquist (complex impedance plane) plot for the $(Ni_{0.36}Nb_{0.24}Zr_{0.40})_{90}H_{10}$ alloy is shown in Fig. 1(a). The alloy's variation of impedance with frequency followed a semi-true circle, showing an ideal Debye relaxation peak. A reactance, R, of 6.6 Ω and a relaxation time, RC_{total}, of 1.2 x 10^{-4} s at the summit of the semicircle were derived from the formula $RC_{total} = 1/(2\pi f_{max})$, where f_{max} (= 1,350 Hz) is the frequency of the peak. Thus, the total capacitance, C_{total}, of
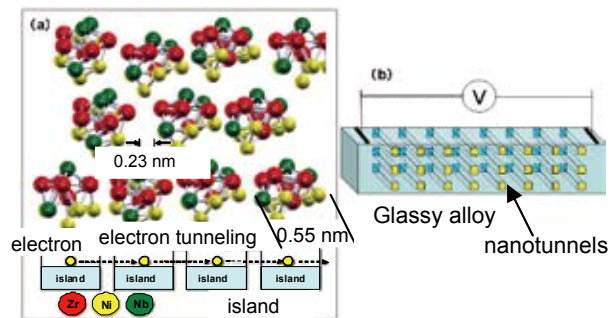

Fig. 2　Configuration pattern of insulating zigzag tunnels among the distorted icosahedral $Zr_5Ni_5Nb_3$ clusters (quantum dot) arranged at intervals of 0.225 nm (a). A glassy alloy has numerous insulating nanotunnels among conducting clusters (b).

the specimen was calculated to be 1.8 x 10^{-5} F.

The Bode plots (b) illustrate the dependencies of the impedance (Z) and phase (θ) on the frequency (f). The impedance and phase remained constant as the frequency rose to 600 and 25,000 Hz, respectively. Then, each of them remarkably decreased as the frequency increased up to 2 MHz: the impedance decreased as a third-order polynomial, and the phase decreased as a parabolic. From these results, we hypothesize the existence of numerous dielectric tunnels in the glassy alloy. Dividing the total capacitance (17.8μF) by the capacitance of a single tunnel (0.9 fF), the number of tunnels was calculated to be 2.0 x 10^{10}. Because the volume of the specimen was 0.60 mm³ (0.04 mm x 1.0 mm x 15 mm), the free volume of 2.57% was 0.015 mm³. Assuming that the tunnel is a regular prism of side d and a length of 15 mm, we obtain the side $d = \sqrt{0.015/2.0E10/15} = 0.225$ nm.

References

[1] M.Fukuhara, M.Seto and A.Inoue, Appl.Phys.Lett., **96**, 043103 (2010).

[2] M.Fukuhara, A.Kawashima,S.Yamaura and A.Inoue, Appl.Phys.Lett., **90**, 20311 (2007).

[3] M.Fukuhara and A.Inoue, J.Appl.Pjys., **105**, 063715 (2009).

[4] M.Fukuhara, N.Fujima, H.Oji, A.Inoue and S.Emura, J. Alloy Comp., **497**, 182 (2010).

Key Words

Nano Quantum Dot Tunnelling, Nanocluster, Nanocapacitor

Contact to

Mikio Fukuhara*

*Present Address: Advanced Materials Development and Integration of Novel Structured Metallic and Inorganic Materials
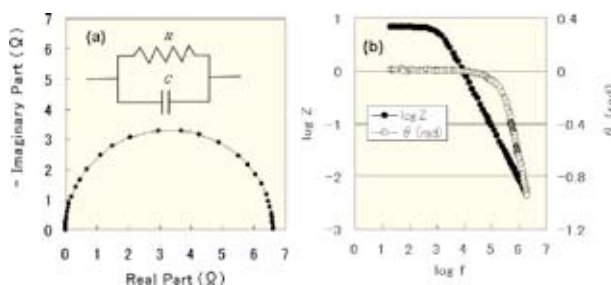E-mail: fukuhara@imr.tohoku.ac.jp

Fig. 1　Nyquist plots (a), and Bode plots showing the impedance (log Z) and the phase (θ) vs the frequency (log f) (b) for the $(Ni_{0.36}Nb_{0.24}Zr_{0.40})_{90}H_{10}$ glassy alloy.

Transport Properties in Ferromagnetic TM-Al-O (TM = Fe, Co) Granular Films with High TM Concentrations

The magnetic and transport properties of TM-Al-O (TM = Fe, Co) granular films strongly depend on the TM concentration. We found that the transport properties of ferromagnetic TM-Al-O films with high TM concentration can be described by the scattering of conduction electrons due to thermally excited ferromagnetic spin waves arising in the strongly coupled granular structure, which is a contrast to the spin-dependent tunneling process observed in superparamagnetic films with low TM concentration.

TM-Al-O (TM = Fe, Co) granular films, consisting of nano-size TM granules and an insulating Al-O matrix, have attracted much attention as materials for various magnetic devices because of their high resistivity and soft magnetization. The magnetic and transport properties strongly depend on the TM concentration x. When x is as low as 40 - 60 at. %, the films are superparamagnetic and exhibit giant magnetic resistance. In this regime, the electrical resistivity ρ increases drastically with decreasing temperature T, following the relation $\ln \rho \propto (1/T)^{1/2}$. With increasing x, the films become ferromagnetic with a soft magnetic property and show a metallic transport property around $x = 60 - 70$ at. %. Until now, the transport mechanism in the superparamagnetic TM-Al-O films is well established to be the spin-dependent electron tunneling between TM granules. However, details of transport properties of ferromagnetic TM-Al-O films have not been fully examined yet. We systematically investigated ρ of them and clarified their characteristic properties [1].

Fe-Al-O and Co-Al-O granular films of 1-2 µm thick, containing Fe (Co) granules with diameter of 2-3 nm, were prepared on glass substrates using radio frequency magnetron sputtering. Figure 1 displays the low temperature ρ of Fe-Al-O films for various x as a function of T^2. We found the relation described as $\rho(T) = \rho(0) + AT^2$ for all the samples in the temperature range of 50 - 150 K with the coefficient A decreasing drastically with increasing x. At temperatures lower than 50 K, ρ deviates from the T^2 behavior, and increases logarithmically according to the formula $\rho(T) = \rho(0)$
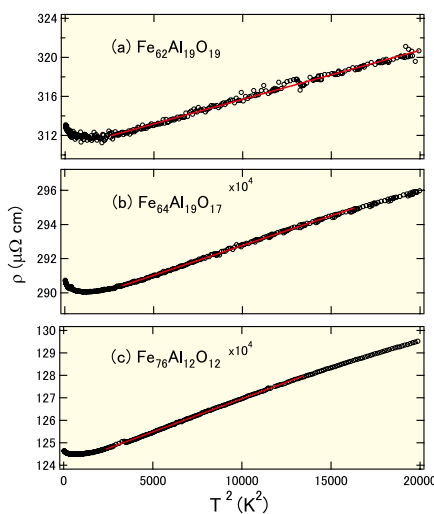

Fig. 1 Temperature dependence of the electrical resistivity of ferromagnetic Fe-Al-O granular films as a function of T^2 for Fe concentrations of (a) 62, (b) 64, (c) 76 at. %. The solid lines are fits to the formula $\rho(T) = \rho(0) + AT^2$.
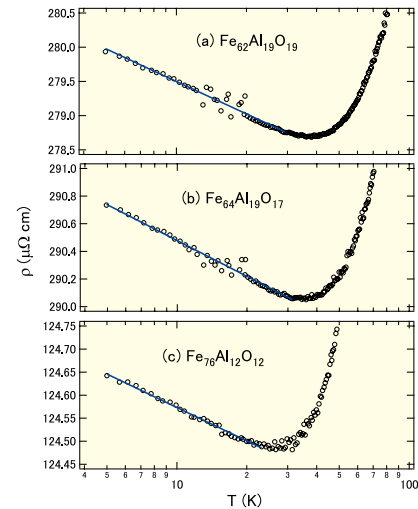

Fig. 2 Temperature dependence of the electrical resistivity of ferromagnetic Fe-Al-O granular films on an expanded log$T$ scale for Fe concentrations of (a) 62, (b) 64, (c) 76 at. %. The solid lines are fits to the formula $\rho(T) = \rho(0) - B\log T$.

– $B\log T$ as shown in Fig. 2. The same types of results were observed also in Co-Al-O films [1]. Therefore, the resistivity described with the combination of T^2 and $-\log T$ terms can be a characteristic of the ferromagnetic TM-Al-O films.

The T^2 behavior is theoretically predicted to occur in pure ferromagnetic metals as a consequence of the scattering of conduction electrons by long spin waves. Recently, Yoshihara *et al*. observed thermally excited spin waves in ferromagnetic TM-Al-O films using Brillouin light scattering (BLS), [2]. The obtained wavelength is about 300 nm, which is much longer than the diameters of granules, leading to the possible existence of the spin waves even in granular system. Since the decrease in the coefficient A with increasing x is consistently related to the increase in the exchange field H_{ex} characterizing the spin wave, which is derived from the analyses of BLS spectra [1,2], the T^2 behavior in the ferromagnetic TM-Al-O films can be ascribed to the scattering of conduction electrons by thermally excited spin waves. This is a good contrast to the spin-dependent tunneling process in superparamagnetic TM-Al-O films. Although the origin of the logarithmic behavior remains open question, we note that this is robust against the magnetic field up to 8 T.

References
[1] S. Nakamura, T. Nojima, A. Yshihara, S. Ohnuma, and H. Fujimori, J. Phys. Soc. Jpn. **78**, 074708 (2009).
[2] A. Yoshihara, S. Ohnuma, H. Fujimori, S. Nakamura and T. Nojima, J. Phys. Soc. Jpn. **77**, 094704 (2008).

Key Words
Ferromagnetic Granular Films, Electrical Resistivity, Spin Wave

Contact to
Tsutomu Nojima (Laboratory of Low Temperature Materials Science)
 E-mail: nojima@imr.tohoku.ac.jp

Ferromagnetism in Semihydrogenated Graphene Sheet

Graphene has been one of the most interesting and exciting discoveries in recent years, which is also be viewed as the next generation of nano-electronic devices. First-principles calculation is a powerful investigation tool to predict and design novel graphene-based nanostructures. The present work showed an interesting behavior of semi-hydrogenated graphene sheet, which possesses uniform 2D ferromagnetism. The method used in this paper is based on density functional theory. All the numerical calculations have been conducted by using the HITACHI SR11000 supercomputer at the Center for Computational Materials Science, IMR.

Fully hydrogenated graphene sheet has been experimentally synthesized. However, studies of magnetic behavior of graphene haven't been achieved to a satisfactory level. With the help of first-principles calculation, geometry, stability, magnetism and electronic structure of semihydrogenated graphene have been predicted. And uniform 2D ferromagnetism can be achieved [1].

Figure 1 shows the optimized geometric structure of semihydrogenated graphene. The sheet has a slightly buckle and the C_1 atoms are sp^3 hybridized, while C_2 atoms are approximated sp^2 hybridized.

Figure 2 shows the spin density of the structure in 2D slice and iso-surface forms. It can be seen that C_2 atoms are ferromagnetically coupled with each other, with magnetism contributed mainly by p_z orbital. Each C_2 atom gives around 1 μ_B magnetic moment. The mechanism of magnetism is due to the broken of delocalized π orbital of graphene by H atoms, thus p_z electrons from unsaturated C_2 atoms are unpaired. States of antiferromagnetism and non-magnetism are energetically unfavorable by 38 meV and 123 meV per unit cell, respectively. And correspondingly, the Curie temperature can be approximated through mean field theory between 278 and 417 K, which shows that the magnetism can be retained under room temperature.

The calculated band structure are plotted in Figure 3, which indicate that the semihydrogenated graphene is an indirect semiconductor, with band gap of ~0.46 eV.
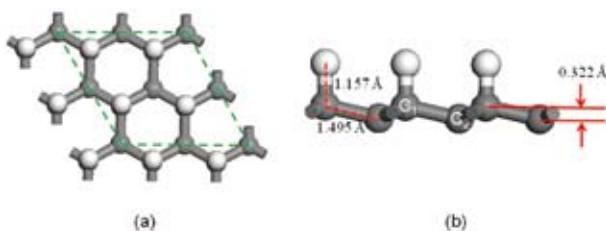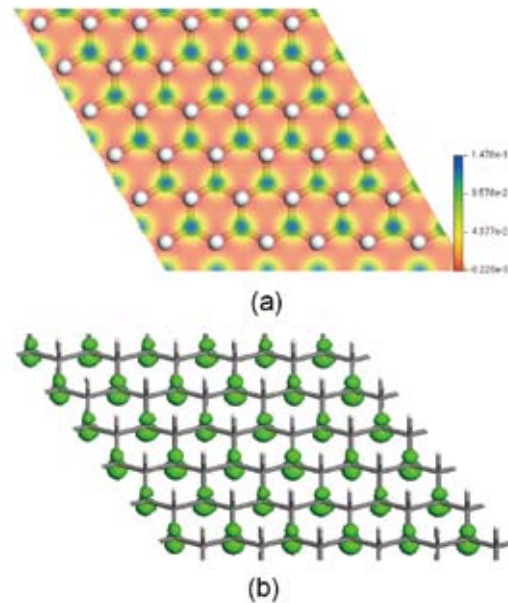

Fig. 2 2D slice and iso-surface of spin density of ferromagnetic semihydrogenated graphene.
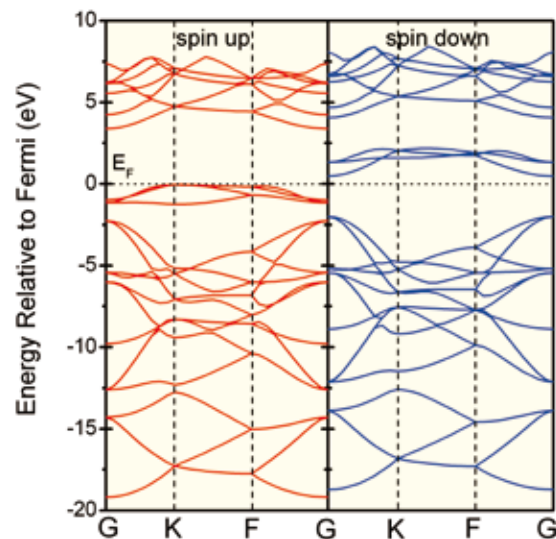

Fig. 3 Electronic band structure of semihydrogenated graphene sheet. G (0, 0, 0), K (-1/3, 2/3, 0), and F (0, 1/2, 0) are high symmetric points in reciprocal space.

Fig. 1 Geometry of semihydrogenated graphene.

References

[1] J. Zhou, Q. Wang, Q. Sun, X. S. Chen, Y. Kawazoe, P. Jena, Nano Lett. **9**, 3867 (2009).

Key Words
Graphene, *ab Initio* Calculation, 2D Ferromagnetic Material

Contact to
Yoshiyuki Kawazoe (Materials Design by Computer Simulation Division)
 E-mail: kawazoe@imr.edu

Possible d^0 Ferromagnetism in MgO Doped with Nitrogen

Using recently developed numerical method we study the possibility of d^0 ferromagnetism in MgO doped with nitrogen. By realistic parameters, we observe a finite local moment for an N impurity, and long-range ferromagnetic correlations between two N impurities. The ferromagnetic correlations are strongly influenced by the impurity bound state [1].

The discovery of ferromagnetism (FM) in dilute magnetic semiconductor (DMS) has created much activity in the field of spintronics. There is the so called d^0 DMS, where the magnetism is coming from moments induced in the p orbitals of the oxygen band instead of from partially filled d orbitals. The experimentally observed d^0 DMS are quite few now. As a promising candidate, the FM in MgO by nitrogen doping has been observed in recent experiment.

Considering the importance of spin and charge fluctuations in d^0 DMS, it is important, therefore, to develop methods which treats correlations correctly and that do not rely on arbitrary approximations or on the separation between charge, spin and orbital fluctuations. Such a method has been introduced and applied to models of the DMS [2], namely combined approach of tight-binding approximation (TBA) or density functional theory (DFT) and Hirsch-Fye quantum Monte Carlo (QMC) method.

When two N impurities are introduced in the MgO host, the magnetic correlation function $<M^z_1M^z_2>$ between $\xi = x$ orbitals of the impurities versus the impurity separation at temperature T = 200 K is shown in Fig. 1. The impurity spins exhibit ferromagnetic (FM) correlations at chemical potential μ = 0.0 eV. By increasing μ to 0.06 eV, the FM correlations become larger, and the range of the FM correlations becomes longer. Further increasing μ, the FM correlations become weaker. This is because the impurity bound states of Mg(O,N) becomes occupied when μ is increased to above 0.06 eV. Results in Fig. 1(b) are obtained with fixed impurity energy ε_p = -0.5 eV. The impurity spins exhibit quite weak antiferromagnetic (AFM) correlations due to the superexchange interaction at μ = 0.0 eV. The impurity bound states of Mg(O,N) lies around 0.35 eV, deep in the band gap (not shown here). Increasing μ to 0.3 eV, the FM correlations appear with stronger magnitude and longer range.

References

[1] B. Gu, N. Bulut, T. Ziman, and S. Maekawa, Phys. Rev. B **79**, 024407 (2009).
[2] B. Gu, N. Bulut, and S. Maekawa, J. Appl. Phys. **104**, 103906 (2008); J. Ohe, Y. Tomoda, N. Bulut, R. Arita, K. Nakamura, and S. Maekewa, J. Phys. Soc. Jpn. **78**, 083703 (2009).

Key Words

Diluted Magnetic Semiconductor, MgO, Quantum Monte Carlo Method

Contact to

Sadamichi Maekawa* (Theory of Solid State Physics Division)
 *Present Address: Advanced Science Research Center, Japan Atomic Energy Agency
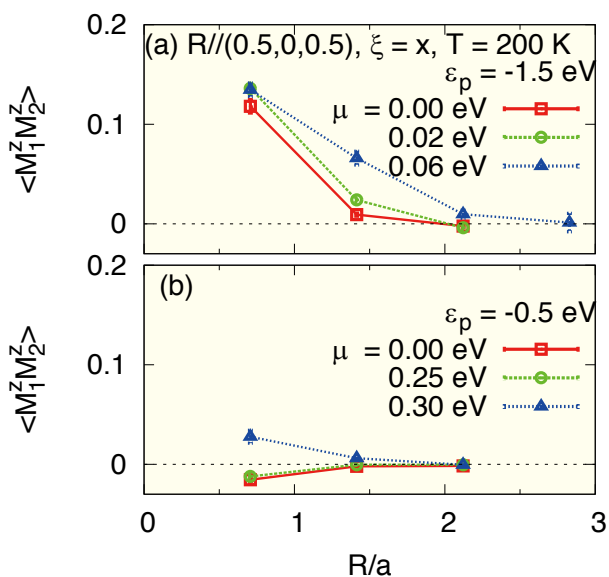 E-mail: maekawa.sadamichi@jaea.go.jp
  URL: http://asrc.jaea.go.jp/

Fig. 1 Magnetic correlation function $<M^z_1M^z_2>$ between $\xi = x$ orbitals of the N impurities versus distance R/a for (a) the impurity 2p energy ε_p= -1.5 eV and (b) ε_p= -0.5 eV at T = 200 K. Direction R//(0.5,0,0.5) is along one of the 12 nearest N-N neighbors in rocksalt structure.